Tellurium-Terminated MXene Synthesis via One-Step Tellurium Etching

Guoliang Ma[1], Zongbin Luo[1], Hui Shao[2] ✉, Yanbin Shen[2], Zifeng Lin[1] ✉,
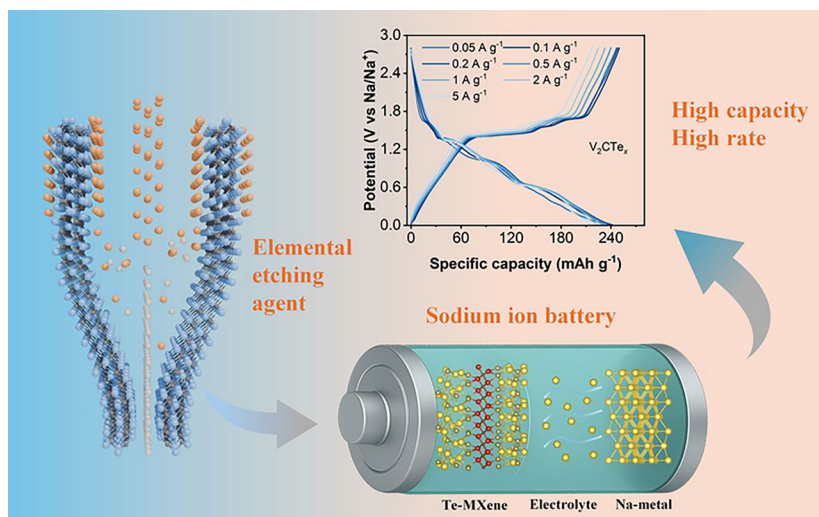Patrice Simon[3] ✉

HIGHLIGHTS

- A novel and efficient Te etching method for the preparation of Te-functionalized MXene materials is presented

- This simple etching method enables the processing of V- and Nb-based MAX phases and demonstrates potential for large-scale production.

- V_2CTe_x MXene has a sodium storage capacity of up to 247 mAh g^{-1} and maintains 216 mAh g^{-1} at 23 C.

ABSTRACT With the rapid development of two-dimensional MXene materials, numerous preparation strategies have been proposed to enhance synthesis efficiency, mitigate environmental impact, and enable scalability for large-scale production. The compound etching approach, which relies on cationic oxidation of the A element of MAX phase precursors while anions typically adsorb onto MXene surfaces as functional groups, remains the main prevalent strategy. By contrast, synthesis methodologies utilizing elemental etching agents have been rarely reported. Here, we report a new elemental tellurium (Te)-based etching strategy for the preparation of MXene materials with tunable surface chemistry. By selectively removing the A-site element in MAX

phases using Te, our approach avoids the use of toxic fluoride reagents and achieves tellurium-terminated surface groups that significantly enhance sodium storage performance. Experimental results show that Te-etched MXene delivers substantially higher capacities (exceeding 50% improvement over conventionally etched MXene) with superior rate capability, retaining high capacity at large current densities and demonstrating over 90% capacity retention after 1000 cycles. This innovative synthetic strategy provides new insight into controllable MXene preparation and performance optimization, while the as-obtained materials hold promises for high-performance sodium-ion batteries and other energy storage systems.

KEYWORDS Te-terminated MXene; Elemental tellurium etching; Sodium-ion storage; High-rate performance

---

✉ Hui Shao, hshao2023@sinano.ac.cn; Zifeng Lin, linzifeng@scu.edu.cn; Patrice Simon, simon@chimie.ups-tlse.fr

1 College of Materials Science and Engineering, Sichuan University, Chengdu 610065, People's Republic of China

2 Lab, CAS Center for Excellence in Nanoscience, Suzhou Institute of Nano-Tech and Nano-Bionics (SINANO), Chinese Academy of Sciences (CAS), Suzhou 215123, People's Republic of China

3 CIRIMAT, Université de Toulouse, CNRS, Toulouse, France

1 Introduction

As nanomaterials research continues to advance rapidly, two-dimensional (2D) materials have become a prominent focus in materials science, owing to their unique layered structures and exceptional physicochemical properties [1, 2]. In particular, MXene-defined by the general formula $M_{n+1}X_nT_x$—where M is a transition metal (e.g., Ti, V, Zr, Cr), X is carbon and/or nitrogen, and T_x represents surface terminations—is a class of transition-metal carbides, nitrides, and carbonitrides with a characteristic layered morphology [3, 4]. Their diverse chemical compositions, high electronic conductivity, and highly tailorable surface functional groups have garnered widespread attention [5, 6]. Since the initial discovery of MXene at 2011 [7], their morphologies have evolved from simple colloidal suspensions to powders and quantum dots [8], offering expanded chemical diversity [9] and extended applications in energy storage [10–17], catalysis [18], electromagnetic shielding [19], sensing [20], and biomedicine [21]. The unique structural and surface chemical features of MXene underpin these remarkable applications, emphasizing the importance of developing effective preparation methods that enable precise control over their surface chemistry [9, 22].

To date, various etching strategies have been developed for MXene synthesis, including wet chemical and high-temperature methods. The conventional approach employs concentrated hydrofluoric acid (HF) to selectively remove the A-layer from MAX phases, enabling the first successful synthesis of MXene [7, 23]. However, this method poses serious safety and environmental risks and typically yields MXene with mixed -F and -OH terminations that are difficult to precisely control. Compared with direct HF etching, this approach is relatively mild and safer, while the concurrent insertion of metal cations and water molecules between layers increases the interlayer spacing and reduces defects. Nevertheless, fluorine-containing reagents remain integral to this process, making it challenging to eliminate -F groups, with potential implications for both environmental impact and the intrinsic properties of MXene [24]. Later, a fluorine-free molten-salt Lewis acid etching method has gained interest [25, 26]. By exploiting molten chlorides (e.g., $CuCl_2$) under an inert atmosphere, the A-site element in MAX phases can be selectively replaced, yielding MXene with primarily Cl terminations [27]. Although this process

avoids toxic fluorides and broadens the range of surface terminations [28], it requires high temperatures in a strongly Lewis-acidic environment, often introducing significant structural defects. Recently, emerging vapor-phase etching approaches have been developed by introducing gaseous elemental halogens (Cl_2, Br_2, I_2) at elevated temperatures in sealed conditions to yield MXene terminated with -Cl, -Br, or -I groups [29]. However, such gas-phase reactions require strict operating conditions and specialized equipment, limiting large-scale deployment. Furthermore, several intriguing environmentally friendly methods for preparing MXene have been reported, such as thermal reduction and ultraviolet-induced etching [30, 31]. Nevertheless, these methods have not comprehensively explored the universal applicability concerning MAX phase precursors. Hence, current etching methods inevitably involve trade-offs in efficiency, safety, and control over the resultant surface terminations, often falling short in achieving the flexible, on-demand synthesis of MXene. Existing strategies typically fix the species of terminal groups to those derived from the chosen reagents, highlighting the challenge of tailoring surface chemistry to optimize MXene performance [32]. To address these shortcomings, "elemental etching" was recently proposed as a potential new pathway, aiming to leverage direct reactions between elemental reagents and MAX precursors to remove the A-layer and introduce targeted functional groups in situ. Compared with conventional fluoride-based acidic etching, elemental etching promises greater flexibility for modulating functional groups, enhanced safety by avoiding strong corrosive acids, and clear thermodynamic driving forces (e.g., forming stable by-products) that could, in principle, enable fine-tuned control over MXene surface chemistry. Although research in this direction remains in its infancy—with limited systematic process optimization and performance evaluation, the approach offers exciting opportunities for overcoming the limitations of traditional techniques.

Herein, we propose a Te-based elemental etching strategy for synthesizing MXene from MAX phases. We find that direct reaction between Te and the MAX precursor at elevated temperatures simultaneously enables selective removal of the A-layer (Al in this work) and in situ formation of Te-containing surface groups on the resultant MXene. Compared with conventional multi-step processes, our single-step strategy eliminates the need for additional surface functionalization steps, thereby greatly simplifying the synthesis. In contrast to halogen-based etching methods, where

halogen elements are typically in the gaseous phase during the reaction, Te exists in the liquid phase under the reaction conditions, offering lower processing requirements and improved controllability. Moreover, Te functionalization not only expands the interlayer spacing and reduces structural defects but also preserves high electrical conductivity owing to the relatively low electronegativity of Te. As a result, the as-prepared MXene exhibits excellent electrochemical performance and structural stability. Moreover, the Te-based etching process delivers a high yield of approximately 77% and exhibits excellent batch-to-batch reproducibility. The method is readily scalable and applicable to the synthesis of a wide range of MXene from different MAX phases. Although Te is a relatively less abundant element, it can be sourced from industrial by-products, and its consumption in this process remains well-controlled. Moreover, the utilized Te can be readily recovered via electrochemical reduction, enabling sustainable material recycling for potential scale-up. Benefiting from synergistic improvements in structure and surface properties, Te-terminated MXene deliver outstanding sodium-ion storage performance. Notably, V_2CTe_x exhibits an excellent capacity of 247 mAh g^{-1}, retaining 216 mAh g^{-1} at a 23 C rate. Overall, our Te-based elemental etching method represents a new avenue for the controllable synthesis of high-performance MXene, holding significant promise for both fundamental research and practical energy storage applications.

2 Experimental Section

2.1 Synthesis of Te-MXene

The preparation of Te-based MXene materials primarily involves mixing various MAX phases with elemental Te. Then, they are held in an Ar gas tube furnace at 700 °C for 1–2 h. Detailed preparation process can be found on supporting materials.

2.2 Preparation of Te-MXene Anode

The electrode was prepared by mixing the MXene material, conductive additive (acetylene black), and binder (PVDF) in a weight ratio of 8:1:1. The mixture was homogenized using N-methyl-2-pyrrolidone (NMP) as the solvent and then coated onto carbon-coated copper foil. The coated foil was dried

at 110 °C for 12 h and subsequently punched into circular disks (12 mm in diameter) for use as electrodes. The active material loading on the MXene electrode was approximately 1.0–1.5 mg cm^{-2}. The electrolyte volume used per cell was approximately 110 μL.

2.3 Theoretical Calculation

The theoretical calculations based on density functional theory (DFT) were performed using the DS-PAW software package integrated within Device Studio [33]. Detailed preparation process can be found on supporting materials.

2.4 Electrochemical Test

All electrochemical measurements were taken using CR2032 coin cells. For the counter electrode, lithium metal foil or sodium metal foil was used. In lithium-ion battery tests, glass fiber (GF/A) was employed as the separator, while GF/D was used in sodium-ion battery tests. The electrolyte for lithium-ion batteries was 1 m $LiPF_6$ in a mixture of ethylene carbonate (EC) and dimethyl carbonate (DMC), and for sodium-ion batteries, 1 m $NaPF_6$ in 1,2-dimethoxyethane (DME) was used. All cells underwent activation treatment at a current density of 20 mA g^{-1} before rate performance, long-cycle, and full-cell tests. For half-cell tests, the voltage range was set between 0.01 and 2.8 V. The assembly of all cells was performed in an argon-filled glove box to ensure an inert atmosphere. Electrochemical tests were primarily conducted using a Neware eight-channel battery testing system (CT-4008 T). All tests were performed in a temperature-controlled chamber (MJS-DZ250, Nanjing Mojiesi) maintained at 27 °C.

3 Results and Discussion

3.1 Principles of Te-MXene Material Preparation

A schematic illustration of the proposed elemental etching reaction (X = Te/Se/S/P…) for selectively converting MAX into MXene is depicted in Fig. 1a. Distinct from conventional compound-based etching systems, this method features a direct redox reaction between the elemental etchant X and the A-site element in a sealed environment, resulting in the formation of X_xA_y compounds and enabling the selective removal of the A-site

species. Meanwhile, the etching element X interacts with the exposed transition-metal (M) atoms on the MXene surface, leading to the formation of X-rich surface terminations. This elementary one-step etching process provides a rational design principle for the precise modulation of MXene surface chemistry. To assess the thermodynamic feasibility, we first constructed a Gibbs free energy (ΔG) model for reactions between elemental X and typical A-site elements (Al, Ga, In, Zn, Pb, Sn, Ge) at 700 °C (Fig. 1b). For Te, ΔG is markedly negative for most A-site element candidates (e.g., $\Delta G = -276.96$ kJ mol^{-1} for Al), indicating a highly spontaneous reaction. Temperature-dependent calculations (Figs. 1b and S1) reveal that for the Al-containing MAX system, ΔG is largest (most negative) at higher temperatures, consistent with the preferential removal of Al in molten Lewis salts. DFT calculations for the model Ti_3AlC_2 system (Fig. 1c, d, e, f and g) indicate that the Te atom strongly adsorbs near the Al site (with an adsorption energy of -2.63 eV), accompanied by pronounced charge transfer. This strong electronic interaction favors fast redox coupling and likely leads to the formation of intermediate Te_xAl_y phases, ultimately driving selective Al removal. Notably, while Te exhibits a lower adsorption energy on Ti_3C_2 (-3.61 eV) compared with –OH

(-4.32 eV) or –O (-6.38 eV), as shown in Fig. 1h. This indicates that to get Te-terminated MXene conventional etching routes would require additional post-treatment steps to displace original functional groups (e.g., high-temperature substitution [34]), since the formation of Te groups is kinetically unfavored in situ. Using elemental Te as the etching reagent could direct formation of the desired Te functional groups during the etching process, highlighting advantages in both simplicity and controllability.

3.2 Te-MXene Material Characterization

We first systematically investigated the reaction mechanism and process optimization for Te-mediated conversion of Ti_3AlC_2 into MXene. To systematically optimize the synthesis conditions, we investigated a range of parameters, including the Te/Ti_3AlC_2 molar ratio (1:1–4:1), reaction temperature (500–900 °C), and holding time (0–6 h). Solid-state reactions under Ar revealed incomplete removal of Al for Te/Ti_3AlC_2 ratios below 3:1, as evidenced by the characteristic (002) and (104) diffraction peaks at 9.6° and 39.1°, respectively (Fig. S2). Excess Te (4:1) resulted in secondary phase formation of $TiTe_2$. Consequently, 3:1 provided optimal stoichiometric balance, ensuring complete etching while
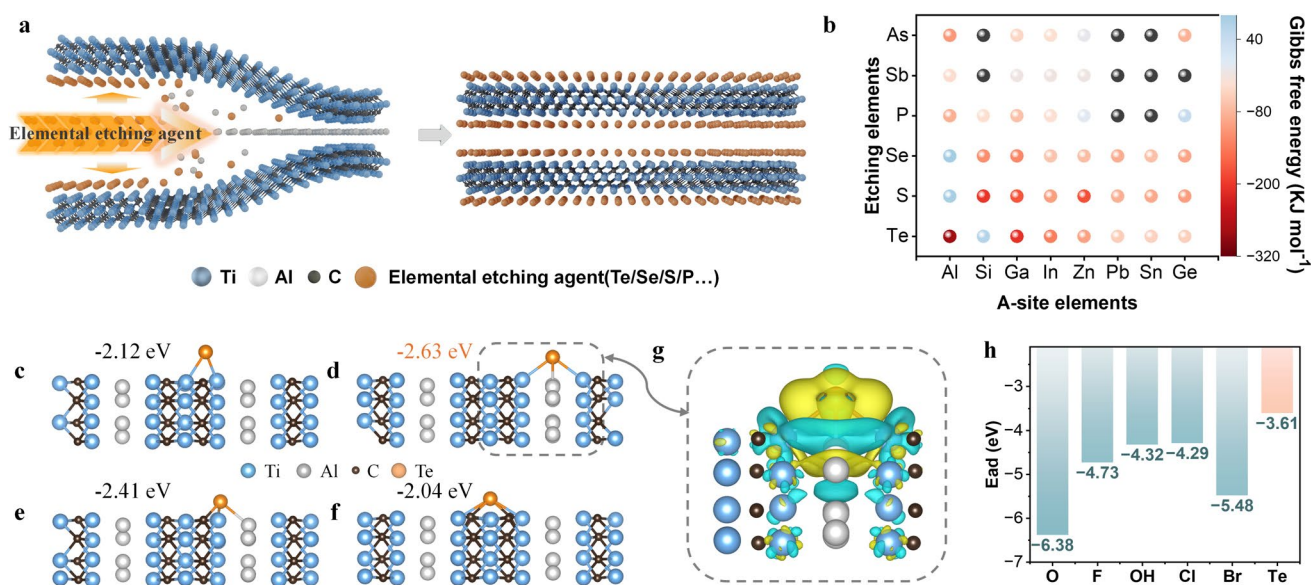

Fig. 1 Principles of MXene synthesis. **a** Schematic illustration of MXene materials prepared by element etching. **b** Gibbs free energies of reaction for various A-site elements (Al, Si, Ga, In, Zn, Pb, Sn, Ge) reacting with Te, S, Se, P, Sb, and As at 700 °C. Adsorption energies of Te at distinct sites of Ti_3AlC_2, including **c** top-C, **d** top-Al, **e** top-Ti1, **f** top-Ti2. **g** Theoretical calculation of differential charge at the Al site following Te adsorption on Ti_3AlC_2. **h** Adsorption energies of different functional groups of Ti_3C_2

minimizing by-product formation. Temperature dependence (Fig. S3a) further indicated that effective etching occurs above 452 °C (the melting point of Te), suggesting a low reaction barrier. Balancing reaction kinetics and efficiency, 700 °C was identified as the optimal temperature for producing high-quality MXene. Moreover, as shown in Fig. S3b, excellent etching performance can be achieved even with a very short reaction time, indicating highly favorable and rapid reaction kinetics. Figure 2a presents the X-ray diffraction (XRD) pattern of the final product obtained at a Te/Ti$_3$AlC$_2$ molar ratio of 3:1 and 700 °C, after HCl washing, alongside that of the Ti$_3$AlC$_2$ precursor for comparison. The absence of characteristic Ti$_3$AlC$_2$ peaks indicates the successful removal of Al, while the pronounced (00 l) reflections confirm the formation of MXene layers. The (002) peak of the Te-functionalized Ti$_3$C$_2$Te$_x$ phase is observed at 6.99°, with a derived interlayer spacing of 12.64 Å. The attenuated intensity of the (002) reflection suggests weakened periodicity along the c-axis, commonly observed in MXene with larger or more complex functional groups. Compared to conventional Ti$_3$C$_2$Cl$_2$ and Ti$_3$C$_2$Br$_2$, the Te-terminated Ti$_3$C$_2$Te$_x$ exhibits an expanded interlayer spacing, which facilitates enhanced ion diffusion and improved electrolyte accessibility (Fig. S4). Moreover, Ti$_3$C$_2$Te$_x$ maintains a high electrical conductivity (45 S m^{-1}, 20 MPa), thereby ensuring efficient charge transport within the electrode. SEM images (Figs. 2b, c and S5) reveal the hallmark accordion-like morphology of MXene after Te etching, with uniformly expanded layers across the sample, indicating efficient and homogeneous etching. Notably, compared with samples from HF or Lewis-acidic melts, the Te-etched MXene exhibits more pronounced accordion-like morphology, implying enhanced interlayer separation with minimal damage to the M-X skeleton. Energy-dispersive spectroscopy (EDS) mapping (Fig. S6) confirms uniform Te distribution. Minor Al$_2$Te$_3$ and residual Te impurities were detected (Fig. S7), which was reduced after HCl washing, yielding to cleaner surface and more prominent MXene reflections. Element quantification analysis suggests a final composition of Ti$_3$C$_{1.69}$Te$_{2.93}$O$_{0.64}$. Figure 2d-f presents high-resolution X-ray photoelectron spectroscopy (XPS) spectra for Ti, C, and Te, unveiling chemical bonding states and compositions on the MXene surface. The Ti-C bond at ~454.92 eV (Ti 2p) and 281.97 eV (C 1s) remains prominent, demonstrating the preservation of the Ti$_3$C$_2$ framework without significant structural disruption. In the Te 3d spectra, the Te^{2-} signals

at 572.95 eV (3$d_{5/2}$) and 583.33 eV (3$d_{3/2}$) corroborate the formation of Ti-Te bonding. The Te-Ti signal significantly outweighs any Te–O peak, indicating that in situ incorporation of Te leads to a higher fraction of Ti-Te bonds compared to previously reported two-step processes [34, 35]. The remaining elemental spectral information is shown in Fig. S8. This suggests reduced oxide formation, improved sample purity, and enhanced retention of the desirable Te-terminated structure. On the other hand, as shown in Fig. S9, a comparison of the samples stored under ambient air conditions for 9 months revealed that both the XRD patterns and microstructure remained nearly unchanged, indicating that the Te-functionalized MXene exhibits excellent environmental stability.

High-angle annular dark-field scanning transmission electron microscopy (HAADF-STEM) images and EDS line scans (Fig. 2g, h) further validate the successful etching of Al, with minimal residual content. Observing along the [11 $\overline{2}$ 0] zone axis, Ti and Te atoms alternate along the c-axis, and the heavier Te atoms appear with enhanced contrast. A structural schematic (Fig. 2i) illustrates the spatial distribution of the elements, consistent with the measured interlayer spacing of ~ 12.9 Å. Theoretical diffraction analysis (Fig. 2a) indicates that Ti$_3$C$_2$Te$_x$ exhibits a (002) reflection at 6.91° (d-spacing ~ 12.78 Å), closely matching our experimental observations. In contrast, Ti$_3$C$_2$Cl$_2$ synthesized via Lewis-acidic melts shows the (002) peak at 7.96° (d-spacing ~ 11.09 Å) (Fig. S10). Hence, the Te-terminated MXene produced here possesses a notably larger interlayer spacing, which should be beneficial for electrochemical ion insertion and other applications [28]. Moreover, first-principles calculations reveal that Ti$_3$C$_2$Te$_x$ has a work function and electronic structure indicative of high conductivity (Fig. 2j), exceeding that of halogen-functionalized MXene and only slightly below that of -OH-functionalized MXene. These results highlight the exceptional conductive properties of Te-terminated MXene.

Based on previously discussed Gibbs free energy calculations and our experimental findings, we propose the etching reaction to process by chemical equation (Eq. 1), which highlights the multifunctional role of Te in the etching mechanism and the formation of MXene materials:
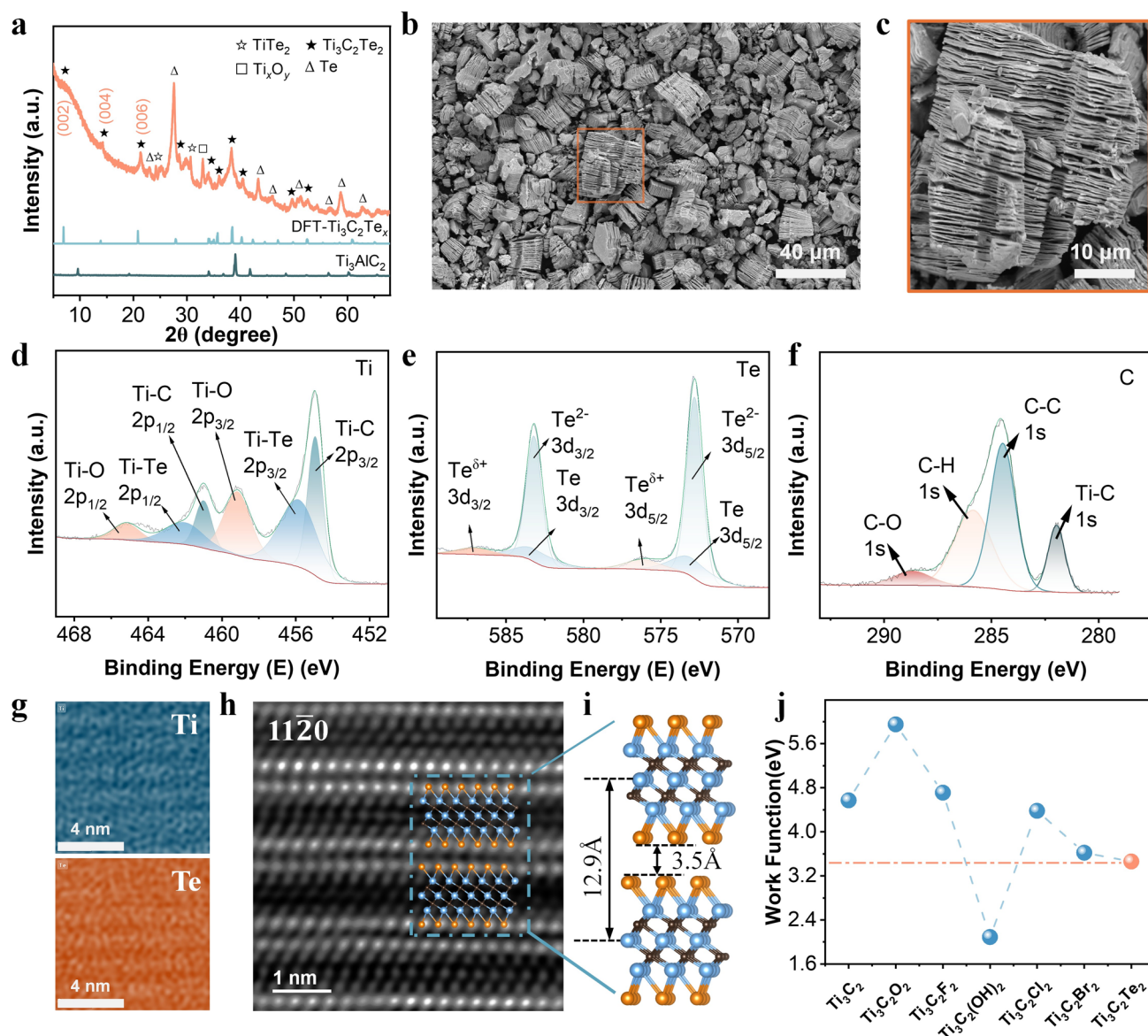
$$2Ti_3AlC_2 + (3 + 2x)Te = 2Ti_3C_2Te_x + Al_2Te_3 \qquad (1)$$
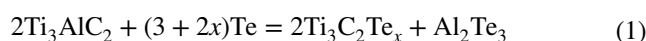
Fig. 2 $Ti_3C_2Te_x$ MXene characterization. **a** XRD patterns of Ti_3AlC_2 MAX phase and $Ti_3C_2T_x$ obtained from experimental characterization and theoretical calculation. **b-c** SEM images of $Ti_3C_2Te_x$. XPS spectra of $Ti_3C_2Te_x$ MXene highlighting **d** Ti, **e** Te, and **f** C. **g** STEM-based elemental mapping revealing Ti and Te distributions. **h** Spherical aberration-corrected TEM image along [11$\bar{2}$0] zone axis, **i** Schematic representation of the atomic structure. **j** Calculated work functions of Ti_3C_2 with different functional groups

3.3 Generalization of the Te Etching Method

Next, we investigated the generalization of the Te-based etching strategy using various MAX precursors, including V_2AlC, Nb_2AlC, and Ti_2AlC. Under optimized conditions (Te/MAX = 3:1, 700 °C, Ar), selective removal of Al was confirmed in all cases (Figs. 3 and S12–S17), as evidenced by the disappearance of MAX diffraction peaks and the emergence of typical MXene reflections. The resulting

powders displayed the characteristic accordion-like morphology. This approach is particularly advantageous for V- and Nb-based MAX systems, where conventional Lewis-acidic etching frequently yields low-quality MXene with a high level of impurities and severe oxidation (Fig. S11). In contrast, Te-based etching provides notably higher material quality and crystallinity. DFT calculations (Fig. 3c, f, i) confirm that V_2CTe_x, Nb_2CTe_x, and Ti_2CTe_x are all structurally stable with Te groups adsorbed primarily atop the metal or

carbon layers, enhancing structural integrity. The analysis of the calculated density of states suggests high electron density near the Fermi level, indicative of good electrical conductivity, a critical advantage for energy storage applications. These findings underscore the versatility of Te-based MXene, whose superior conductivity, stability, and tunable surface features could be exploited for a wide array of functional applications.

We further broaden the scope of this synthetic route by extending it to the etching of 211-(Ti_2AlN, Cr_2AlC, Ta_2AlC), 312-(Ti_3AlCN), and 413-type (Ti_4AlN_3 and V_4AlC_3) of MAX phases. As shown in Figs. 4 and S18–S25, XRD and SEM data confirm effective etching across these diverse compositions, consistent with thermodynamic predictions

that favor Al removal. Notably, only elemental Te and the MAX powder are required, both of which are stable under ambient conditions, which is an important practical advantage for large-scale manufacturing. More interestingly, upscaling the etching reaction to ~40-fold batches (20 g) resulted in comparable Te-terminated MXene quality as evidenced by SEM and XRD characterizations (Fig. 4h, i), confirming that this Te-based etching route is well suited for large-scale production. Furthermore, based on the preceding thermodynamic analysis, we explored the etching behavior of Se and S toward Ti_3SiC_2 (Fig. S26). The results show that Se effectively etched Ti_3SiC_2, while S failed to achieve etching due to its highly volatile nature during the process.
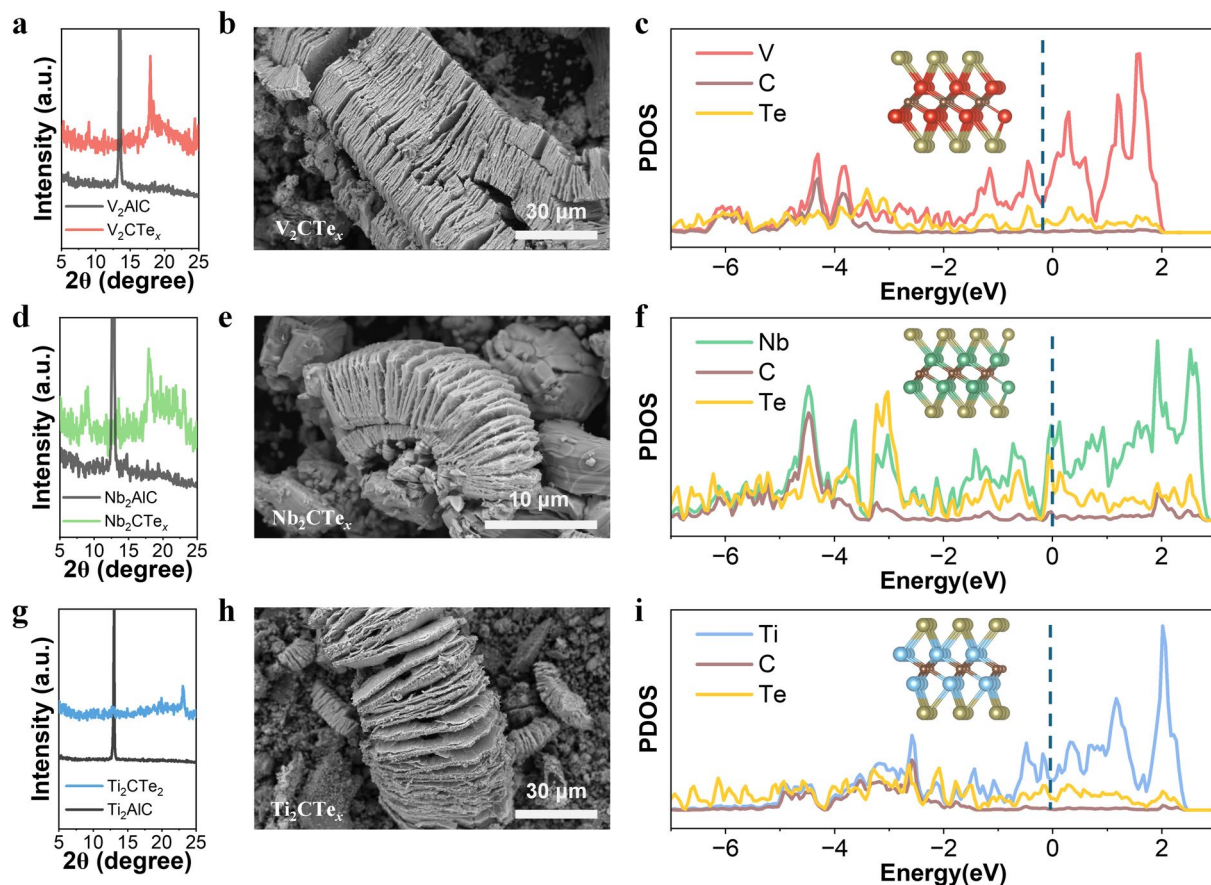

Fig. 3 Preparation of various MXene. **a** XRD patterns of V_2AlC and V_2CTe_x MXene, **b** SEM image of V_2CTe_x MXene before acid washing, and **c** theoretical calculation of optimized structure and projected density of states curve. **d** XRD patterns of Nb_2AlC and Nb_2CTe_x MXene, **e** SEM image of Nb_2CTe_x MXene before acid washing, and **f** theoretical calculation of optimized structure and projected density of states curve. **g** XRD patterns of Ti_2AlC and Ti_2CTe_x MXene, **h** SEM image of Ti_2CTe_x MXene before acid washing, and **i** theoretical calculation of optimized structure and projected density of states curve
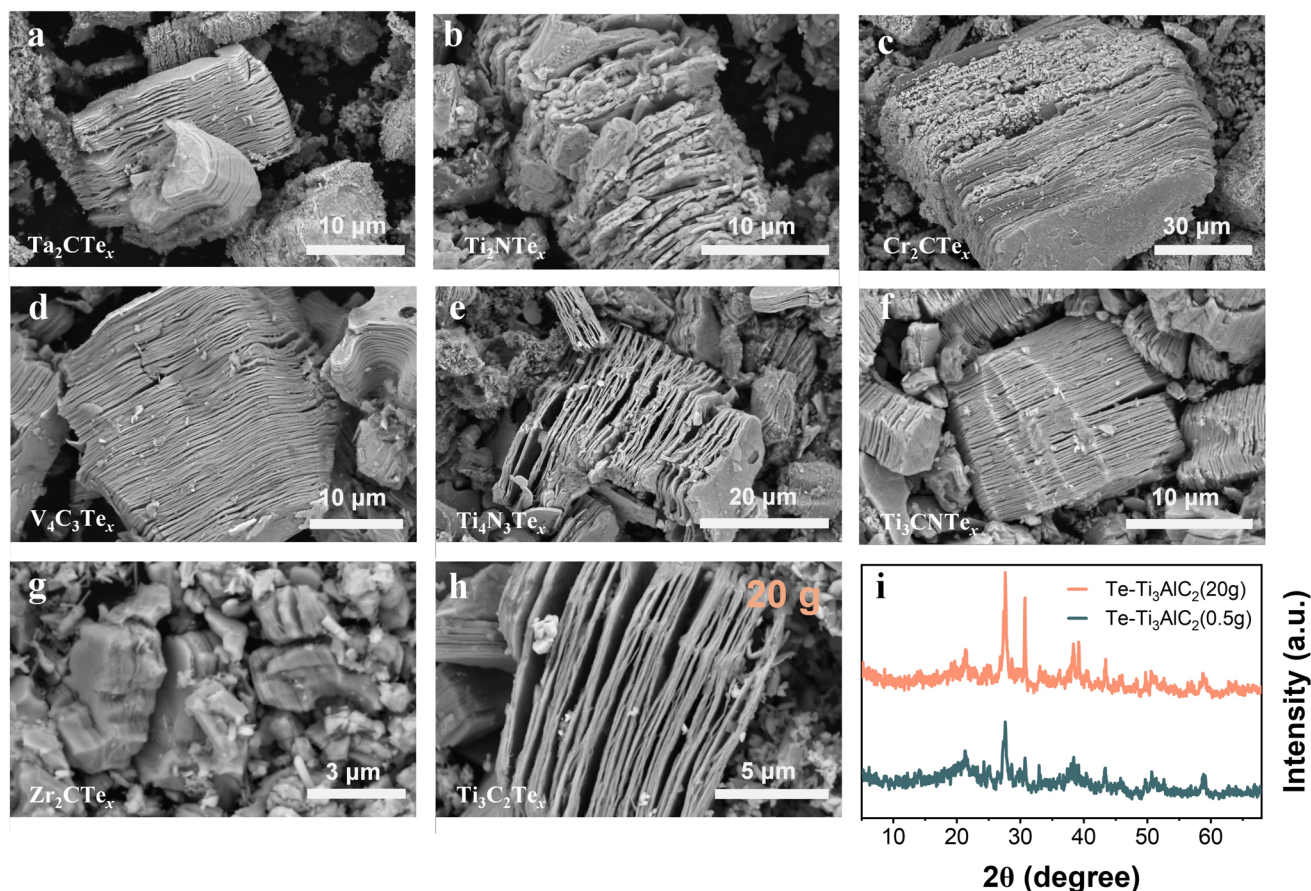
Fig. 4 Universality and batch characterization. SEM images demonstrating the successful Te-based etching of various MAX phases, **a** Ta_2CTe_x. **b** Ti_2NTe_x. **c** Cr_2CTe_x. **d** $V_4C_3Te_x$. **e** $Ti_4N_3Te_x$. **f** Ti_3CNTe_x. **g** Zr_2CTe_x. Batch preparation of $Ti_3C_2Te_x$ MXene. **h** SEM image and **i** XRD pattern of the product

3.4 Te-MXene Material for Sodium Storage

To elucidate how Te terminations influence electrochemical behavior, we achieved the electrochemical characterizations of Te-functionalized MXene during Na-ions intercalation [36]. Figure 5a compares the reversible charge storage capacity and rate performance of $Ti_3C_2Te_x$, $Ti_3C_2Br_2$, $Ti_3C_2Cl_2$, and $Ti_3C_2F_2$ at various current densities. At a current density of 0.05 A g^{-1}, $Ti_3C_2Cl_2$ delivers a capacity of 137 mAh g^{-1}, while $Ti_3C_2Te_x$ achieves a higher capacity of 180 mAh g^{-1}. Moreover, $Ti_3C_2Te_x$ retains 89% of its capacity (160 mAh g^{-1}) at high specific current of 2 A g^{-1}, whereas the Cl-terminated MXene shows only 44% capacity retention under the same conditions. In contrast, the overall electrochemical performance of $Ti_3C_2Br_2$ and $Ti_3C_2F_2$ is poor. The lithium-ion storage performance of Te-functionalized MXene was evaluated. As shown in Fig.

S27, both types of Te-terminated MXene materials exhibit rapid capacity fading and poor cycling stability when used as electrodes in lithium-ion batteries. This inferior performance is likely due to the absence of the Na-Te alloying mechanism that plays a key role in enhancing capacity and cycling stability in sodium-ion systems. The observations highlight that Te functionalities not only increase the storage capacity but also markedly enhance the rate capability of MXene electrodes in sodium-ion batteries. We further investigated the electrochemical behavior of four different Te-functionalized MXene ($Ti_3C_2Te_x$, V_2CTe_x, Ti_2CTe_x, and Nb_2CTe_x), compared with the elemental Te (Fig. 5b). Their charge–discharge profiles show a distinctive plateau around 1.5 V vs. Na$^+$/Na commonly associated with Na-Te alloying, which is corroborated by differential capacity (dQ/dV) curves (Fig. S28). Among these, V_2CTe_x delivers the highest capacity of 247 mAh g^{-1}. Figure 5c, d depicts typical
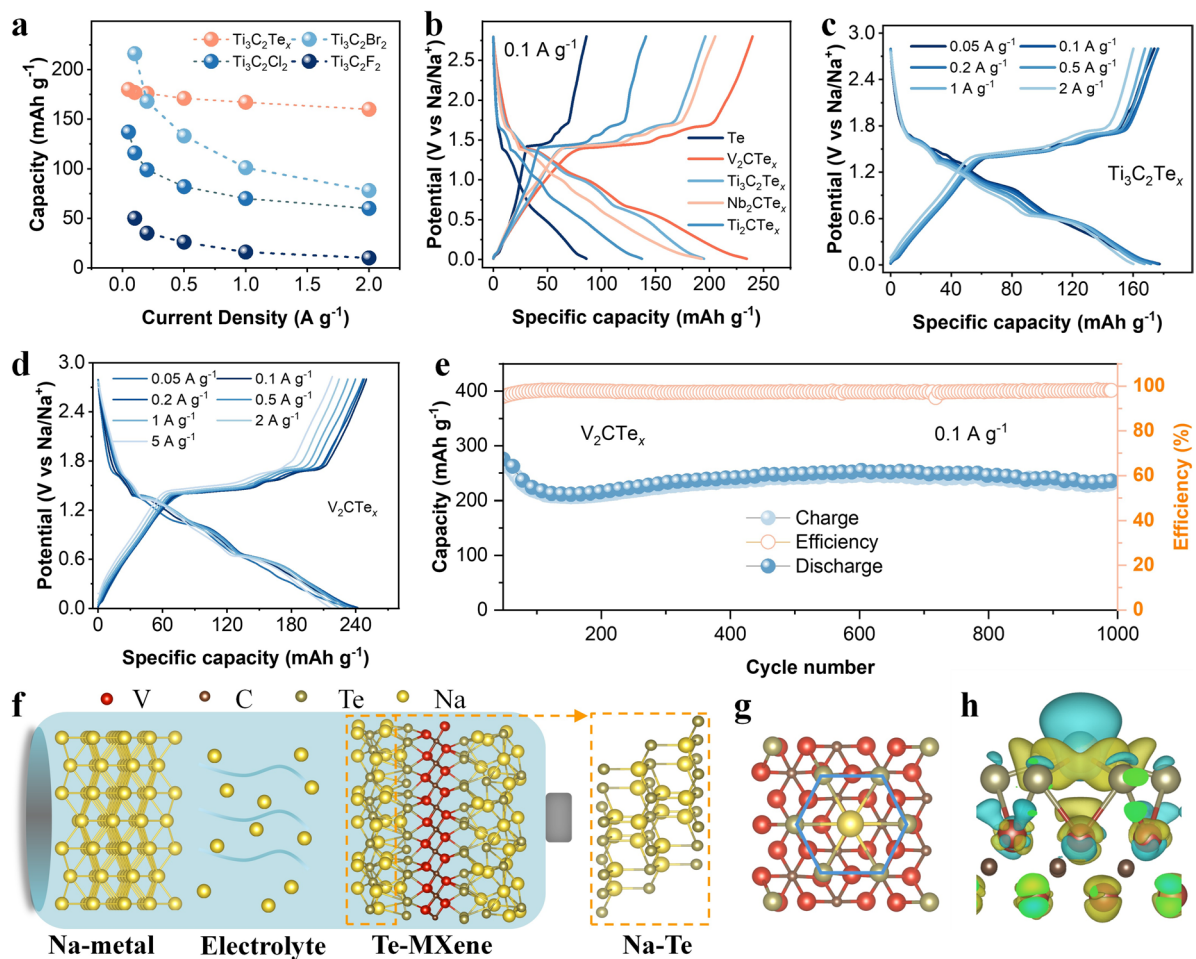
Fig. 5 Sodium storage properties of Te-MXene. **a** Electrochemical performance comparison of sodium storage for $Ti_3C_2Te_x$, $Ti_3C_2Br_2$, $Ti_3C_2Cl_2$ and $Ti_3C_2F_2$. **b** Charge and discharge profiles of Te-based MXene electrodes at 0.1 A g^{-1}. Rate-dependent charge and discharge curves of **c** $Ti_3C_2Te_x$ and **d** V_2CTe_x. **e** Long-cycle stability of V_2CTe_x at 0.1 A g^{-1}. **f** Proposed storage mechanism for Te-based MXene materials. **g** Top-view depiction of optimized V_2CTe_x MXene electrode material surface. **h** Differential charge distribution for Na adsorption at Te functional group vacancies on the surface of the V_2CTe_x MXene electrode material

charge–discharge curves at various rates for $Ti_3C_2Te_x$ and V_2CTe_x, respectively, demonstrating excellent rate performance with minimal polarization. Even at 5 A g^{-1} (corresponding to 23 C-rate), V_2CTe_x retains 216 mAh g^{-1}. Long cycling of V_2CTe_x at 0.1 A g^{-1} reveals capacities above 235 mAh g^{-1} after 1000 cycles, underscoring outstanding cyclic stability. Even under high current cycling at 2 A g^{-1} (Fig. S29), the V_2CTe_x electrode exhibited excellent cycling stability. Compared to conventional hard carbon materials, the Te-functionalized MXene exhibits superior rate capability and a higher voltage plateau, which not only contributes to higher power density but also helps effectively avoid dendrite formation during cycling. Previous studies have

shown that tellurium undergoes a Na-Te alloying process in sodium-ion batteries [37, 38]. However, Te-based negative electrodes often suffer from large volumetric changes during alloying/dealloying, leading to structural instability. In addition, we conducted sodium storage tests on pure Te electrodes within this system. As shown in Fig. S30, the overall capacity was relatively low and exhibited continuous fading during cycling. Here, the surface-bound nature of Te on 2D MXene scaffolds is believed to provide a promising solution (Figs. 5g and S31a, b), in which the alloying reaction may predominantly involve Te groups that partially detach from the MXene surface to form Na-Te [38], thereby helping to preserve the layered MXene framework and reduce

mechanical degradation. As shown in Fig. S32, post-cycling disassembly of the V_2CTe_x-based cell revealed that the primary species deposited on the separator was Na-Te alloy, which is consistent with the previous analytical results. DFT calculations (Figs. 5h and S31c, d) further indicate that Na ions react preferentially with surface Te groups, leaving behind vacancies on the MXene surface, which can subsequently absorb additional Na. The post-cycling SEM observations revealed that the V_2CTe_x electrode still retained a well-defined layered morphology, indicating good structural stability during long-term cycling. X-ray photoelectron spectroscopy (XPS) analysis was conducted on the V_2CTe_x electrode after cycling in the discharged state. The Te spectrum is presented in Fig. S33. Compared with the pristine V_2CTe_x, the Te functional group content significantly decreased, as indicated by the marked reduction in Te peak intensity. This is attributed to the partial desorption or transformation of Te functional groups during electrochemical cycling, resulting in a reduced surface content. Moreover, a distinct Te-Na bonding peak appeared at approximately 572 eV, further confirming that after the detachment of Te functional groups, the resulting Te vacancies can effectively facilitate Na^+ adsorption and bonding. These findings are in good agreement with the results of the ex-situ XRD analysis and the analysis of products on the separator surface. These insights underscore that Te-based MXene uniquely integrates the advantages of 2D layered architectures with the high capacity contributions of chalcogenide alloying, thereby delivering exceptional performance and stability in sodium-ion storage. The assembled full cell exhibited a specific capacity of 104 mAh g^{-1} at 0.1 A g^{-1} (Fig. S34), with a voltage profile positioned between the average voltages of the cathode and anode in their respective half-cells. Collectively, these electrochemical results highlight the significant potential of Te-based MXene materials for high-performance sodium-ion batteries and further advance the practical deployment of MXene-based materials in next-generation energy storage systems.

4 Conclusion

In summary, we present a controllable synthesis strategy for MXene based on elemental Te, which leverages the redox reactivity of Te to achieve simultaneous selective etching of Al from the MAX phase and in situ Te functionalization. Compared with conventional methods, this one-step approach obviates additional surface functionalization steps and markedly simplifies synthesis. Our results demonstrate the broad applicability and scalability of the Te-based route across multiple MAX systems, consistently yielding Te-terminated MXene with well-defined "accordion-like" morphologies. The introduction of Te functional groups endows MXene with enhanced structural stability, larger interlayer spacing, and improved electrical conductivity, leading to substantially boosted electrochemical sodium-ion storage performance. V_2CTe_x achieves 247 mAh g^{-1} at 0.05 A g^{-1} and retains 216 mAh g^{-1} even at 2 A g^{-1} (23 C). Our findings indicate that elemental etching, exemplified here by Te, offers a new paradigm for tuning MXene surface chemistry and optimizing device-level performance, underscoring the fundamental importance and far-reaching potential of MXene in energy storage applications.

Author Contributions P.S., Z.F.L., and H.S. initiated and supervised the work. G.L.M. conducted the primary material synthesis, characterization, and electrochemical testing, as well as data analysis. Z.B.L. contributed to the experiments and analysis related to the electrochemical data analysis. P.S., Z.F.L, H.S., and G.L.M. prepared the manuscript, and all authors reviewed and edited the final version.

Declarations

Conflict of Interest The authors declare no interest conflict. They have no known competing financial interests or personal relationships that could have appeared to influence the work reported in this paper.

References

1. R. Yang, L. Mei, Z. Lin, Y. Fan, J. Lim et al., Intercalation in 2D materials and *in situ* studies. Nat. Rev. Chem. **8**(6), 410–432 (2024). https://doi.org/10.1038/s41570-024-00605-2

2. J. Zhou, Z. Lin, H. Ren, X. Duan, I. Shakir et al., Layered intercalation materials. Adv. Mater. **33**(25), e2004557 (2021). https://doi.org/10.1002/adma.202004557

3. A. VahidMohammadi, J. Rosen, Y. Gogotsi, The world of two-dimensional carbides and nitrides (MXenes). Science (2021). https://doi.org/10.1126/science.abf1581

4. H. Ding, Y. Li, M. Li, Z. Chai, Q. Huang, Layered transition metal carbides/nitrides: from chemical etching to chemical editing. Acc. Mater. Res. **6**(1), 28–39 (2025). https://doi.org/10.1021/accountsmr.4c00250

5. M. Naguib, M.W. Barsoum, Y. Gogotsi, Ten years of progress in the synthesis and development of MXenes. Adv. Mater. **33**(39), e2103393 (2021). https://doi.org/10.1002/adma.202103393

6. J.L. Hart, K. Hantanasirisakul, A.C. Lang, B. Anasori, D. Pinto et al., Control of MXenes' electronic properties through termination and intercalation. Nat. Commun. **10**(1), 522 (2019). https://doi.org/10.1038/s41467-018-08169-8

7. M. Naguib, M. Kurtoglu, V. Presser, J. Lu, J. Niu et al., Two-dimensional nanocrystals produced by exfoliation of Ti_3AlC_2. Adv. Mater. **23**(37), 4248–4253 (2011). https://doi.org/10.1002/adma.201102306

8. C. Guan, X. Yue, J. Fan, Q. Xiang, MXene quantum dots of Ti_3C_2: Properties, synthesis, and energy-related applications. Chin. J. Catal. **43**(10), 2484–2499 (2022). https://doi.org/10.1016/S1872-2067(22)64102-0

9. K.R.G. Lim, M. Shekhirev, B.C. Wyatt, B. Anasori, Y. Gogotsi et al., Fundamentals of MXene synthesis. Nat. Synth **1**(8), 601–614 (2022). https://doi.org/10.1038/s44160-022-00104-6

10. B. Anasori, M.R. Lukatskaya, Y. Gogotsi, 2D metal carbides and nitrides (MXenes) for energy storage. Nat. Rev. Mater. **2**(2), 16098 (2017). https://doi.org/10.1038/natrevmats.2016.98

11. P. Das, Z.-S. Wu, MXene for energy storage: present status and future perspectives. J. Phys. Energy **2**(3), 032004 (2020). https://doi.org/10.1088/2515-7655/ab9b1d

12. X. Li, Z. Huang, C.E. Shuck, G. Liang, Y. Gogotsi et al., MXene chemistry, electrochemistry and energy storage applications. Nat. Rev. Chem. **6**(6), 389–404 (2022). https://doi.org/10.1038/s41570-022-00384-8

13. X. Xu, L. Yang, W. Zheng, H. Zhang, F. Wu et al., MXenes with applications in supercapacitors and secondary batteries: a comprehensive review. Mater. Rep. Energy **2**(1), 100080 (2022). https://doi.org/10.1016/j.matre.2022.100080

14. X. Gao, Y. Liu, M. Shen, X. Liu, Y. Zhao et al., Gas-phase conversion promising controlled construction of functional ZnF_2/V_2CTx for stabilizing Zn metal anodes toward aqueous zinc-ion batteries. Adv. Funct. Mater. (2025). https://doi.org/10.1002/adfm.202503212

15. Y. Liu, X. Gao, M. Shen, Y. Zhao, X. Zhang et al., *In-situ* construction of functional multi-dimensional MXene-based composites directly from MAX phases through gas-solid reactions. Angew. Chem. Int. Ed. **63**(52), e202412898 (2024). https://doi.org/10.1002/anie.202412898

16. J. Zhang, R. Jia, K.B. Tan, J. Li, S. Xu et al., A review of MAX series materials: from diversity, synthesis, prediction, properties oriented to functions. Nano-Micro Lett. **17**(1), 173 (2025). https://doi.org/10.1007/s40820-025-01673-9

17. X. Zuo, Y. Qiu, M. Zhen, D. Liu, Y. Zhang, Review on MXenes-based electrocatalysts for high-energy-density lithium-sulfur batteries. Nano-Micro Lett. **17**(1), 209 (2025). https://doi.org/10.1007/s40820-025-01726-z

18. Z. Kang, M.A. Khan, Y. Gong, R. Javed, Y. Xu et al., Recent progress of MXenes and MXene-based nanomaterials for the electrocatalytic hydrogen evolution reaction. J. Mater. Chem. A **9**(10), 6089–6108 (2021). https://doi.org/10.1039/D0TA11735H

19. A. Iqbal, P. Sambyal, C.M. Koo, 2D MXenes for electromagnetic shielding: a review. Adv. Funct. Mater. **30**(47), 2000883 (2020). https://doi.org/10.1002/adfm.202000883

20. D.H. Ho, Y.Y. Choi, S.B. Jo, J.-M. Myoung, J.H. Cho, Sensing with MXenes: progress and prospects. Adv. Mater. **33**(47), 2005846 (2021). https://doi.org/10.1002/adma.202005846

21. A. Maleki, M. Ghomi, N. Nikfarjam, M. Akbari, E. Sharifi et al., Biomedical applications of MXene-integrated composites: regenerative medicine, infection therapy, cancer treatment, and biosensing. Adv. Funct. Mater. **32**(34), 2203430 (2022). https://doi.org/10.1002/adfm.202203430

22. B.C. Wyatt, A. Rosenkranz, B. Anasori, 2D MXenes: tunable mechanical and tribological properties. Adv. Mater. **33**(17), 2007973 (2021). https://doi.org/10.1002/adma.202007973

23. M. Ghidiu, M.R. Lukatskaya, M.-Q. Zhao, Y. Gogotsi, M.W. Barsoum, Conductive two-dimensional titanium carbide 'clay' with high volumetric capacitance. Nature **516**(7529), 78–81 (2014). https://doi.org/10.1038/nature13970

24. C.E. Shuck, K. Ventura-Martinez, A. Goad, S. Uzun, M. Shekhirev et al., Safe synthesis of MAX and MXene: guidelines to reduce risk during synthesis. ACS Chem. Health Saf. **28**(5), 326–338 (2021). https://doi.org/10.1021/acs.chas.1c00051

25. Y. Li, H. Shao, Z. Lin, J. Lu, L. Liu et al., A general Lewis acidic etching route for preparing MXenes with enhanced electrochemical performance in non-aqueous electrolyte. Nat. Mater. **19**(8), 894–899 (2020). https://doi.org/10.1038/s41563-020-0657-0

26. M. Li, J. Lu, K. Luo, Y. Li, K. Chang et al., Element replacement approach by reaction with lewis acidic molten salts to synthesize nanolaminated MAX phases and MXenes. J. Am.

Chem. Soc. **141**(11), 4730–4737 (2019). https://doi.org/10.1021/jacs.9b00574

27. G. Ma, H. Shao, J. Xu, Y. Liu, Q. Huang et al., Li-ion storage properties of two-dimensional titanium-carbide synthesized *via* fast one-pot method in air atmosphere. Nat. Commun. **12**(1), 5085 (2021). https://doi.org/10.1038/s41467-021-25306-y

28. J. Chen, Q. Jin, Y. Li, H. Shao, P. Liu et al., Molten salt-shielded synthesis (MS³) of MXenes in air. Energy Environ. Mater. **6**(2), e12328 (2023). https://doi.org/10.1002/eem2.12328

29. J. Zhu, S. Zhu, Z. Cui, Z. Li, S. Wu et al., Solvent-free one-step green synthesis of MXenes by "gas-phase selective etching." Energy Storage Mater. **70**, 103503 (2024). https://doi.org/10.1016/j.ensm.2024.103503

30. J. Mei, G.A. Ayoko, C. Hu, Z. Sun, Thermal reduction of sulfur-containing MAX phase for MXene production. Chem. Eng. J. **395**, 125111 (2020). https://doi.org/10.1016/j.cej.2020.125111

31. J. Mei, G.A. Ayoko, C. Hu, J.M. Bell, Z. Sun, Two-dimensional fluorine-free mesoporous Mo_2C MXene *via* UV-induced selective etching of Mo_2Ga_2C for energy storage. Sustain. Mater. Technol. **25**, e00156 (2020). https://doi.org/10.1016/j.susmat.2020.e00156

32. S. Munir, A. Rasheed, T. Rasheed, I. Ayman, S. Ajmal et al., Exploring the influence of critical parameters for the effective synthesis of high-quality 2D MXene. ACS Omega **5**(41), 26845–26854 (2020). https://doi.org/10.1021/acsomega.0c03970

33. P. Blöchl, Projector augmented-wave method. Phys. Rev. B **50**(24), 17953–17979 (1994). https://doi.org/10.1103/physrevb.50.17953

34. V. Kamysbayev, A.S. Filatov, H. Hu, X. Rui, F. Lagunas et al., Covalent surface modifications and superconductivity of two-dimensional metal carbide MXenes. Science **369**(6506), 979–983 (2020). https://doi.org/10.1126/science.aba8311

35. H. Ding, Y. Li, M. Li, K. Chen, K. Liang et al., Chemical *Scissor*-mediated structural editing of layered transition metal carbides. Science **379**(6637), 1130–1135 (2023). https://doi.org/10.1126/science.add5901

36. L. Dai, J. Zhao, Q. Li, M. Chen, H. Li et al., Understanding the tunable sodium storage performance in pillared MXenes: a first-principles study. Phys. Chem. Chem. Phys. **24**(44), 27184–27194 (2022). https://doi.org/10.1039/D2CP02961H

37. S. Dong, D. Yu, J. Yang, L. Jiang, J. Wang et al., Tellurium: a high-volumetric-capacity potassium-ion battery electrode material. Adv. Mater. **32**(23), e1908027 (2020). https://doi.org/10.1002/adma.201908027

38. H. Fan, P. Mao, H. Sun, Y. Wang, S.S. Mofarah et al., Recent advances of metal telluride anodes for high-performance lithium/sodium-ion batteries. Mater. Horiz. **9**(2), 524–546 (2022). https://doi.org/10.1039/d1mh01587g